APPLIED SCIENCES AND ENGINEERING

Active recruitment of anti–PD-1–conjugated platelets through tumor-selective thrombosis for enhanced anticancer immunotherapy

Yixin Wang[1,2,3], Wen Li[1], Zhaoting Li[1,2,3], Fanyi Mo[1], Yu Chen[1,2,3], Mari Iida[4], Deric L Wheeler[4], Quanyin Hu[1,2,3]*

Immune checkpoint inhibitors (ICIs) can reinvigorate T cells to eradicate tumor cells, showing great potential in combating various types of tumors. We propose a delivery strategy to enhance tumor-selective ICI accumulation, which leverages the responsiveness of platelets and platelet-derivatives to coagulation cascade signals. A fused protein tTF-RGD targets tumor angiogenic blood vessel endothelial cells and initiates the coagulation locoregionally at the tumor site, forming a "cellular hive" to recruit anti–PD-1 antibody (aPD-1)–conjugated platelets to the tumor site and subsequently activating platelets to release aPD-1 antibody to reactivate T cells for improved immunotherapy. Moreover, on a patient-derived xenograft breast cancer model, the platelet membrane–coated nanoparticles can also respond to the coagulation signals initiated by tTF-RGD, thus enhancing the accumulation and antitumor efficacy of the loaded chemotherapeutics. Our study illustrates a versatile platform technology to enhance the local accumulation of ICIs and chemodrugs by taking advantage of the responsiveness of platelets and platelet derivatives to thrombosis.

INTRODUCTION

Immune checkpoint blockade (ICB)–based immunotherapy has revolutionized the paradigm of tumor therapy (*1*, *2*). Blocking the interaction between checkpoint receptors on immune cells and their ligands on tumor cells with immune checkpoint inhibitors (ICIs) contributes to the restoration of T cell function for eradicating tumors. However, the clinical application of ICIs has been associated with various immune-related adverse events (irAEs) and varied objective response rates (*3*, *4*). Moreover, although encouraging therapeutic outcomes have been achieved in the combination ICB therapy with anti–programmed cell death 1/programmed cell death ligand-1 (PD-1/PD-L1) and anti–cytotoxic T-lymphocyte–associated protein 4 monoclonal antibodies, it is also reported to induce more toxicity (*5*–*7*). The antibodies administered via conventional systemic routes do not preferentially accumulate in the tumor area, resulting in off-target binding to normal tissues, which may cause severe irAEs and compromise the therapeutic efficacy. Besides, previous studies have validated that the therapeutic efficacy of ICIs largely depends on how they are delivered, and locoregional administration such as intratumoral injection contributed to longer tumor retention and robust systemic antitumoral immunity compared to intraperitoneal injection (*8*). Moreover, the reduction in the required dose by intratumoral injection will minimize the potential off-target toxicities on normal tissues.

Although the intratumoral injection is a direct route that guarantees the access of drugs to tumor sites and is widely adopted in animal-based studies, the difficulties in the implementation of intratumoral injection to deep-seated tumors or tumors with small volumes restrict its application in the clinic (*9*). Besides, this administration strategy relies on the skills of professionals and the guidance of imaging techniques (*10*). Active targeting delivery systems, most of which are designed on the basis of ligand-receptor interaction, in which specific ligands are decorated on the delivery systems to bind to the disease-overexpressing receptors, can achieve site-specific ICI delivery and increase local ICI availability after being administered systemically. However, many receptors are not tumor exclusive and are also present on normal tissues, which may lead to off-target effects and systemic toxicity. Besides, the conventional active targeting strategy does not allow the subsequent accumulation of delivery systems after the saturation of target receptor binding, which may dampen the efficiency of ligand-receptor–oriented delivery systems even with repetitive dosing (*11*–*13*). Therefore, there is a clear and urgent need for the development of platforms that can overcome the limitations of current active targeting strategies for ICI delivery.

Here, we artificially create a "cellular hive" that can navigate anti–PD-1 antibody–conjugated platelets (designated P-aPD-1) homing to the tumor site and unload the therapeutic cargoes locally. Tissue factor (TF), as one initiator of blood coagulation, can activate the extrinsic coagulation pathway and induce the transformation of prothrombin to thrombin, in which process substantial amounts of platelets are recruited to form a thrombus (*14*). To mimic the inherent coagulation process, we synthesized a fusion protein truncated tissue factor–Arg-Gly-Asp (RGD) (tTF-RGD), which is capable of initiating the coagulation cascade upon the interaction between the RGD motif and integrins (such as αvβ3 integrin) on endothelial cells of tumor neovasculature. RGD is an extensively investigated motif that can bind to integrin αvβ3 overexpressed on tumor cells and endothelial cells of tumor neovasculature (*15*). In this design, RGD was leveraged to shuttle tTF to the angiogenic tumor blood vessel to initiate the coagulation signaling cascade, in which this strategy holds the potential to bypass the

[1]Pharmaceutical Sciences Division, School of Pharmacy, University of Wisconsin-Madison, Madison, WI 53705, USA. [2]Carbone Cancer Center, School of Medicine and Public Health, University of Wisconsin-Madison, Madison, WI 53705, USA. [3]Wisconsin Center for NanoBioSystems, School of Pharmacy, University of Wisconsin-Madison, Madison, WI 53705, USA. [4]Department of Human Oncology, University of Wisconsin, Madison, WI 53705, USA.
*Corresponding author. Email: qhu66@wisc.edu

binding saturation, since it only serves as the trigger for thrombus formation rather than achieving maximized therapeutic accumulation in the conventional active targeting delivery system. The tTF-RGD can be injected either by peritumoral (p.t.) or intravenous route to trigger the coagulation cascade only in the tumor region, amplifying the signals to recruit platelets to form a thrombus (Fig. 1A). P-aPD-1 that are injected subsequently can respond to this physiological coagulation signaling, actively participate in the thrombosis, and enrich at the tumor site. The coagulation cascade further triggers the activation of platelet to secrete platelet-derived microparticles (PMPs) and release aPD-1 antibodies within the tumor site to reinvigorate T cells for enhanced immune response. To further extend our treatment strategy to other therapeutic modalities, we encapsulated chemotherapeutics paclitaxel (PTX) in dextran nanoparticles (NPs) and coated them with platelet membrane (PM) to form PM-NP/PTX. Cell membrane inherits many surface receptors from its parent cells, and previous reports demonstrated that cell membrane-cloaked NPs could migrate in response to physiological signals (*16*, *17*). Thus, PM-NP holds the potential to migrate in response to platelet-attracting signals such as tTF-RGD–mediated thrombosis. The enhanced tumor accumulation and antitumoral efficacy were demonstrated on a patient-derived xenograft (PDX) breast cancer model, which substantiated the clinical treatment potential of our treatment approach. Our study presents a promising strategy to enhance the tumor-selective accumulation of various platelet-based therapeutics by initiating thrombosis within the tumor site and can be easily adapted to other treatment modalities. Furthermore, this treatment approach can mimic the physiological signaling cascade to artificially create a tumor-targeting environment, which can enhance the tumor-selective accumulation of therapeutics and bypass the limitations of conventional active targeting strategy.

RESULTS

Synthesis and characterization of fusion protein tTF-RGD

Compared with TF, the factor X (FX) activation activity of tTF that lacks a transmembrane domain is decreased by five orders of magnitude as reported in the literature (*18*). To restore the coagulation-initiating capability of tTF, RGD motif was here adopted as a transmembrane domain to redirect the tTF to tumor neovasculature, which is expected to trigger tumor-selective thrombosis with an improved in vivo biosafety profile compared to TF. The tumor-targeted chimeric protein tTF-RGD was generated by fusing the RGD motif to the extracellular domain of TF. The purity of tTF and tTF-RGD was verified by SDS–polyacrylamide gel electrophoresis (SDS-PAGE; Fig. 1B), which showed more than 96% of purity for both tTF and tTF-RGD. The activity of tTF and tTF-RGD was validated by FX activation assay. As presented in Fig. 1C, both tTF and tTF-RGD exhibited a dose-dependent FX activation activity in the presence of factor VIIa (FVIIa) and Ca^{2+} ions. Moreover, the capability of tTF-RGD to initiate coagulation in vivo was first examined by direct intratumoral injection (Fig. 1D). After 24 hours after injection, the tumors were collected. Severe coagulation was observed in tumors after tTF-RGD treatment, whereas minimal to modest coagulation was observed in tTF-treated tumors. Considering the limited application of the intratumoral injection in the clinical treatment of tumors, we planned to adopt two strategies for in vivo application in which tTF-RGD will be administered via p.t. (local) or intravenous (systemic) routes. As shown in fig. S1, there was an obvious hemorrhage and thrombus formation in the tumors after intratumoral injection of tTF-RGD with a relatively high concentration (1.25 mg/kg), which may impede the infiltration of immune cells and permeation of therapeutic drugs. Thus, in the p.t. injection, we decreased the administration dose of tTF-RGD to 0.4 mg/kg, which effectively triggered obvious coagulation without severe hemorrhage. We further tested whether the intravenous injection of tTF-RGD will be effective in initiating tumor-selective thrombus formation. As shown in fig. S1, tTF-RGD (1.25 mg/kg) every other day for three times injected through intravenous routes did not induce severe hemorrhage but could trigger thrombosis within the tumor. In addition, we compared the tumor-selective coagulation-initiating efficacy of tTF and tTF-RGD, with bovine serum albumin (BSA) serving as the control group. As shown in Fig. 1E, tTF-RGD triggered apparent coagulation, while this phenomenon was not observed after both tTF and BSA treatments. Besides, the hematoxylin and eosin (H&E) staining suggested that there was no obvious hemorrhage or thrombus in other major organs after three doses of intravenously injected tTF-RGD, demonstrating the tumor-selective thrombosis and great in vivo biosafety profile of tTF-RGD (fig. S2). Both tTF and BSA did not trigger coagulation in any organs, including tumor tissues, we hypothesized that it was attributed to the lack of targeting ability and the loss of the transmembrane domain in tTF.

Therefore, we examined the tumor-targeting ability of tTF-RGD. Mice bearing subcutaneous CT26 tumors were injected with Cy5.5-labeled tTF and tTF-RGD via intravenous route and visualized using in vivo imaging systems (IVIS). As shown in Fig. 2A, tTF-RGD group exhibited much stronger tumor targeting capability than tTF, as evidenced by the brighter fluorescence signals at the tumor site during the time course of the treatment. At 24 hours after administration, the tumor tissues were collected and visualized ex vivo, which showed an increased accumulation of tTF-RGD than tTF (Fig. 2B) Quantitatively, the mean fluorescence intensity (MFI) of tumor tissues in the tTF-RGD group was 1.62-fold higher than that in the tTF group (Fig. 2C), substantiating the tumor-targeting ability of tTF-RGD, which was attributed to the RGD binding affinity toward the integrin receptors on the angiogenic blood vessels in the tumor site (*15*). The major organs and tumors were collected at 24 hours after p.t. or intravenous injection of the proteins (fig. S3). After p.t. injection, both tTF and tTF-RGD mainly accumulated in tumor sites, and only limited signals can be observed in the major organs. Although predominant signals were observed in the liver after intravenous injection of the proteins, tTF-RGD showed notably higher fluorescence in tumor tissues than tTF. Next, to investigate the capabilities of tTF-RGD in initiating coagulation, fibrinogen (the precursor of fibrin) was injected via intravenous route right after intravenous injection of BSA or tTF or tTF-RGD (Fig. 2D). TF naturally serves as an initiator of blood coagulation by forming the TF:FVIIa complex, which drives the activation of FX and the subsequent transformation of prothrombin to thrombin (Fig. 2E). Thrombin then converts soluble fibrinogen to insoluble fibrin, which can form clots together with the activated platelets (*19*). We anticipate that the fusion protein tTF-RGD can also initiate the coagulation cascade in a tumor-specific manner. Given that tissue coagulation contributes to the conversion of fibrinogen to fibrin and subsequent deposition of fibrinogen, we used Cy5.5-labeled fibrinogen to characterize the coagulation process in

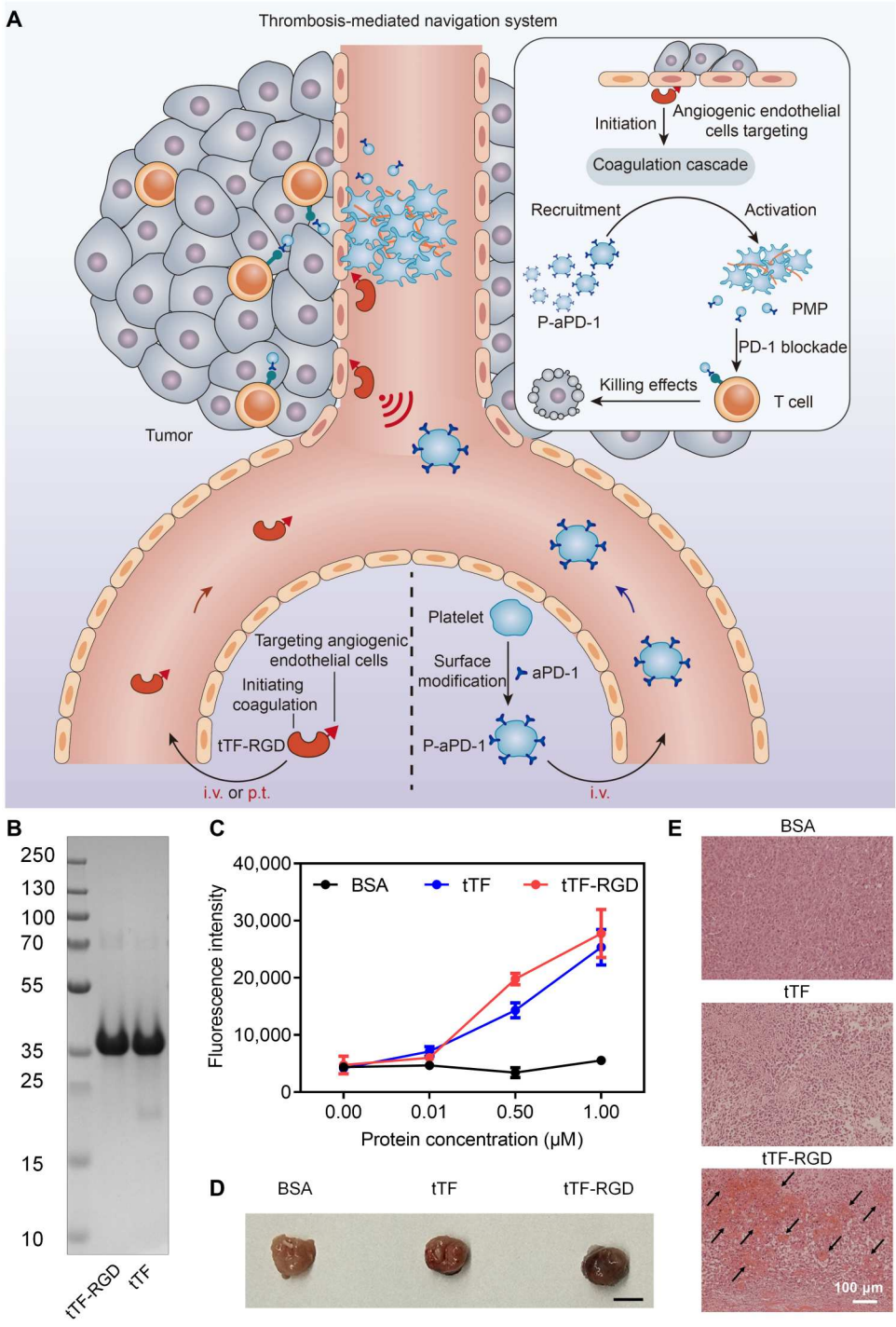

Fig. 1. Characterization of the thrombosis-mediated navigation system. (**A**) Schematic of the thrombosis-mediated navigation system for P-aPD-1. Truncated tissue factor–Arg-Gly-Asp (RGD) (tTF-RGD), administered either by intravenous (i.v.) or p.t. routes, targets tumor neovasculature endothelial cells and initiates coagulation cascade to recruit anti–programmed cell death 1 (PD-1) antibody–conjugated platelets (P-aPD-1). P-aPD-1 is activated during the coagulation process to release aPD-1 in the form of PMP-aPD-1. (**B**) SDS–polyacrylamide gel electrophoresis (SDS-PAGE) analysis of tTF and tTF-RGD. (**C**) Ability of tTF and tTF-RGD to promote the proteolytic activation of factor X (FX) byFVIIa. Data are presented as means ± SEM. $n = 3$. (**D**) Ex vivo photographs of tumor tissues at 24 hours after intratumoral injection of bovine serum albumin (BSA), tTF, and tTF-RGD (dose: 1.25 mg/kg). Scale bar, 5 mm. (**E**) Hematoxylin and eosin (H&E) staining of tumor tissues at 24 hours after three doses of intravenous injection of BSA, tTF, and tTF-RGD (dose: 1.25 mg/kg). Arrow indicates coagulation.

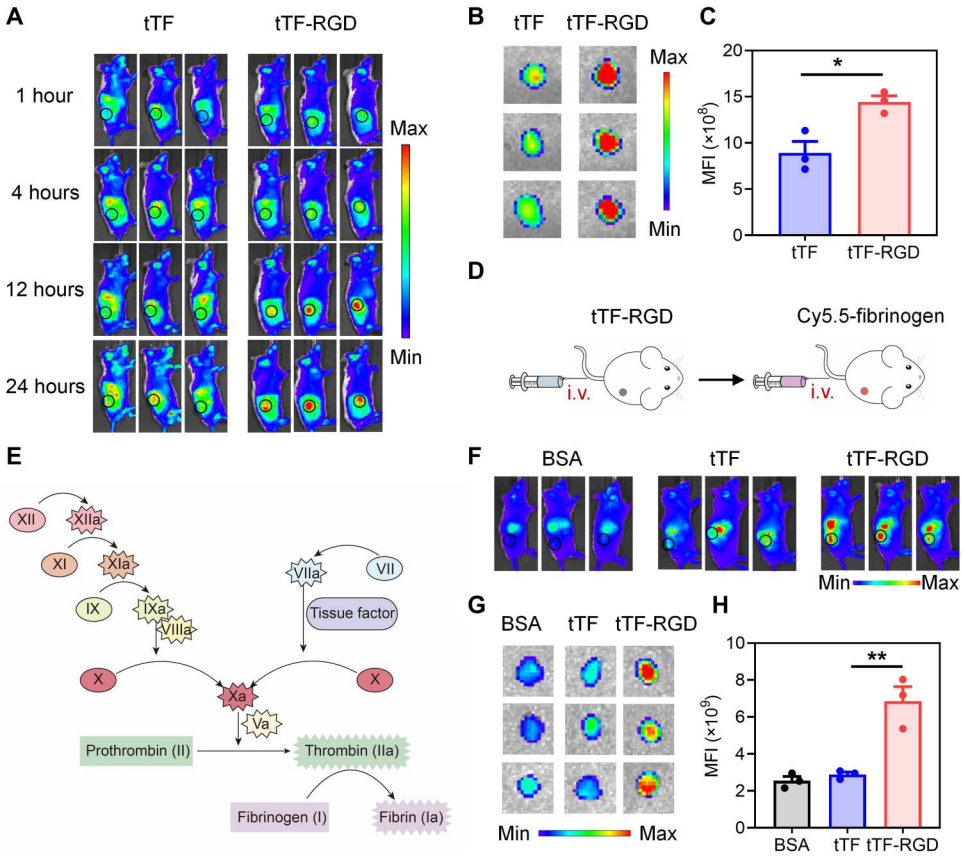

Fig. 2. Characterization of tumor targeting and coagulation initiation capabilities of tTF-RGD. (**A**) Fluorescence imaging of mice at different time points after intravenous (i.v.) injection of Cy5.5-labeled tTF or tTF-RGD ($n = 3$ per group). tTF or tTF-RGD = 1.25 mg/kg. The black circle indicates the tumor site. (**B**) Ex vivo fluorescence imaging of tumor tissues at 24 hours after injection. (**C**) The mean fluorescence intensities (MFIs) of tumors shown in (B). *$P < 0.05$, unpaired Student's t tests. (**D**) Schematic illustration of the experimental design to examine the coagulation initiation capability of tTF-RGD. (**E**) The underlying mechanism of tTF-RGD to trigger the activation of coagulation process and attract fibrinogen. (**F**) Representative fluorescence images showing the biodistribution of Cy5.5-labeled fibrinogen at 24 hours after intravenous injections of BSA, tTF, and tTF-RGD (dose: 1.25 mg/kg, $n = 3$ per group). The black circle indicates the tumor site. (**G**) Ex vivo fluorescence imaging of tumor tissues at 24 hours after injection. (**H**) The MFIs of tumors shown in (G). Data are presented as means ± SEM. **$P < 0.01$, one-way analysis of variance (ANOVA) followed by multiple comparison test.

tumors. At 24 hours after injections of tTF-RGD and Cy5.5-fibrinogen, strong signals were observed in tumors treated with tTF-RGD + fibrinogen group, while fibrinogen did not preferentially accumulate in tumors after BSA or tTF treatment (Fig. 2, F and G). Compared with tTF group, the MFI in tumors after tTF-RGD treatment increased by 2.37-fold (Fig. 2H). The results substantiated that tTF-RGD could effectively induce coagulation to attract fibrinogen at tumor sites.

Recruitment of P-aPD-1 to the tumor site by tTF-RGD

After validating that tTF-RGD is capable of selectively triggering coagulation at tumor sites, we investigated whether administrated P-aPD-1 could take advantage of this process to be actively recruited to the tumor site. Platelets are quick responders to vascular injury and hemorrhage. Besides, after the initiation of the coagulation cascade, the generated thrombin and other signal molecules can activate platelets to aggregate with fibrin to form a platelet plug locally and build up the thrombus (*19*, *20*). Therefore, we anticipated that P-aPD-1 could also selectively accumulate at tumor sites during the tTF-RGD–initiated coagulation. The P-aPD-1 was prepared by conjugating amine groups on the aPD-1 antibodies to the thiol groups on the platelet surface with sulfosuccinimidyl-4-(*N*-maleimidomethyl)cyclohexane-1-carboxylate (Sulfo-SMCC) linkers. The overlap between the red signals from wheat germ agglutinin (WGA) 594–labeled platelets and the green signals from fluorescein isothiocyanate (FITC)–labeled antibodies was observed under the confocal microscope, demonstrating the successful modification of aPD-1 on the platelets (fig. S4). The biofunctionalities of P-aPD-1 were studied by the thrombin-triggered platelet aggregation test and collagen-binding assay. The thrombin-triggered activation of platelets was not altered after aPD-1 decoration, as evidenced by the clot formation in both P-aPD-1 and naïve platelets (fig. S5). In addition, there was no significant difference in the collagen-binding capability of P-aPD-1 in comparison with naïve platelets (fig. S6). Then, the release profiles of the activated and nonactivated P-aPD-1 were studied. We demonstrated that after the activation of platelets by thrombin, about 63.47% of aPD-1 was released within 8 hours, which was substantially higher than that of the nonactivated platelets (16.71%) (fig. S7). These properties demonstrated that P-aPD-1 can still respond to coagulation-related biological signals and release surface-conjugated aPD-1.

Next, we examined whether the in vivo injection of tTF-RGD can recruit P-aPD-1 to the tumor site. Mice bearing CT26 tumors were injected with BSA or tTF or tTF-RGD via p.t. injection, followed by intravenous injection of Cy5.5-labeled P-aPD-1 (Fig. 3A). In the tTF-RGD treatment group, P-aPD-1 showed a strong tendency to accumulate at the tumor site from 4 hours after injection (Fig. 3B). At 24 hours, there is an obvious higher accumulation of P-aPD-1 in the tTF-RGD treatment group than that in either BSA or tTF treatment groups. The ex vivo quantification of tumor tissues demonstrated a 1.87-fold increase in the fluorescence signals of P-aPD-1 in the tTF-RGD group than that in the tTF group, substantiating that p.t. injection of tTF-RGD can attract P-aPD-1 to the tumor site by triggering tumor-selective thrombus formation (Fig. 3, C and D).

Having verified that tTF-RGD can target tumor area and local delivery of tTF-RGD can attract P-aPD-1 to the tumor area, we further tested whether intravenous injection of tTF-RGD can also recruit P-aPD-1 to the tumor site. Cy5.5-labeled P-aPD-1 was given via intravenous route after the intravenous injection of tTF-RGD (Fig. 3E). As consistent with the previous finding in p.t. injection

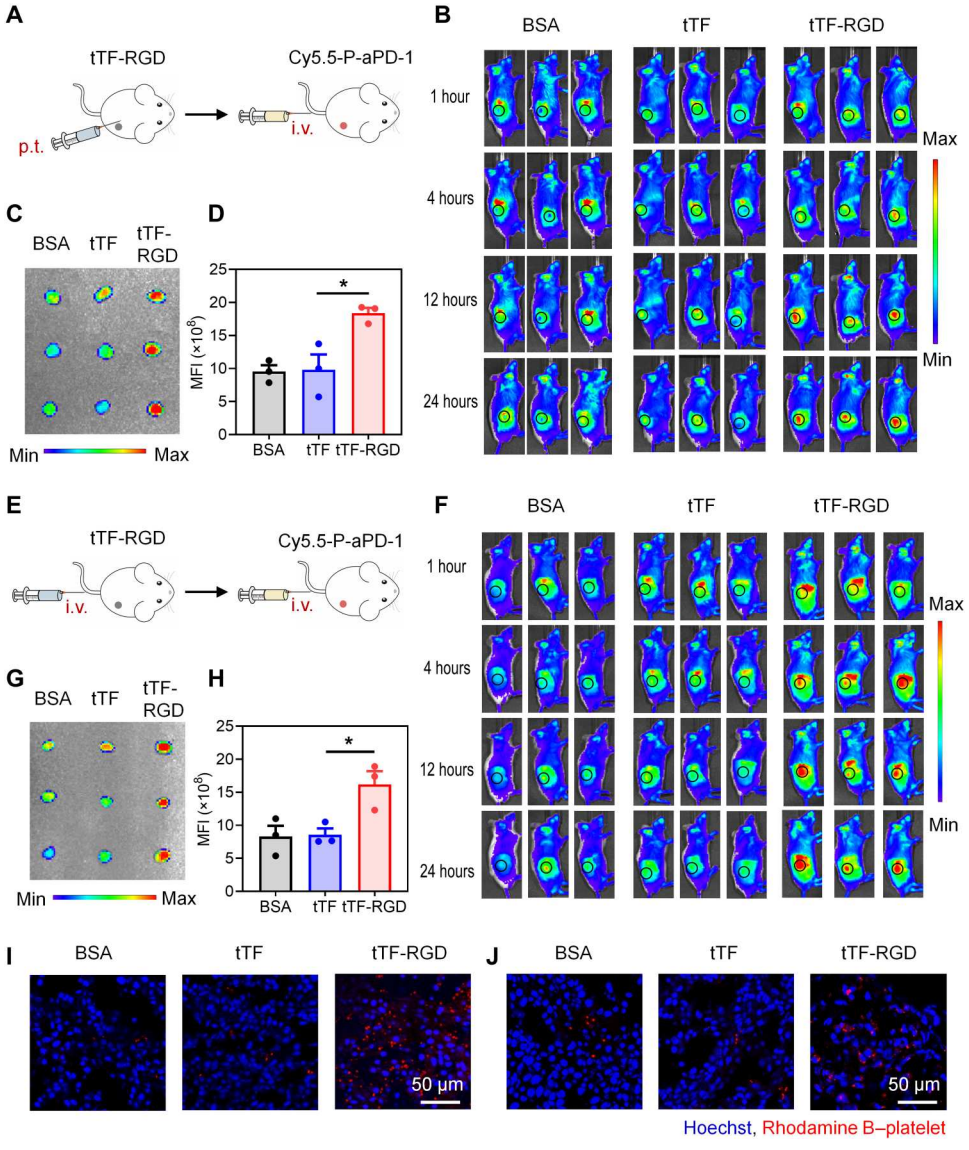

Fig. 3. Characterization of platelet recruitment capabilities of tTF-RGD. (**A**) Schematic illustration of the experimental design to examine the recruitment of P-aPD-1 to tumor areas after p.t. injection of tTF-RGD. (**B**) Fluorescence imaging of mice at different time points after p.t. injection of BSA, tTF, and tTF-RGD at the dose of 0.4 mg/kg, followed by the intravenous injection of Cy5.5-labeled P-aPD-1 (platelet number: 1×10^8, $n = 3$ per group). The black circle indicates the tumor site. (**C**) Ex vivo fluorescence imaging of tumor tissues at 24 hours after injection. (**D**) The MFIs of tumors shown in (C). *$P < 0.05$, one-way ANOVA, followed by multiple comparison test. (**E**) Schematic illustration of the experimental design to examine the recruitment of P-aPD-1 to tumor areas after intravenous (i.v.) injection of tTF-RGD. (**F**) Fluorescence imaging of mice at different time points after intravenous injection of BSA, tTF, and tTF-RGD at the dose of 1.25 mg/kg, followed by the intravenous injection of Cy5.5-P-aPD-1 (platelet number: 1×10^8, $n = 3$ per group). The black circle indicates the tumor site. (**G**) Ex vivo fluorescence imaging of tumor tissues at 24 hours after injection. (**H**) The MFIs of tumors shown in (G). Data are presented as means ± SEM. *$P < 0.05$, one-way ANOVA followed by multiple comparison test. (**I** and **J**) Accumulation of P-aPD-1 in tumors collected from mice treated with p.t. injected BSA/tTF/tTF-RGD + intravenously injected P-aPD-1 (I) or intravenously injected BSA/tTF/tTF-RGD + intravenously injected P-aPD-1 (J).

of tTF-RGD, the intravenous injection of tTF-RGD also induced an increased distribution of P-aPD-1 at the tumor site compared to tTF and BSA treatments during the time course of IVIS monitoring (Fig. 3F), leading to a 1.89-fold increase in the accumulation of P-aPD-1 in the tumor tissue in the tTF-RGD group than that in the tTF group at 24 hours after administration (Fig. 3, G and H). We further labeled P-aPD-1 with rhodamine B and examined the distribution of P-aPD-1 in tumors collected from mice that received the treatment of the local and systemic strategies with tTF-RGD. More fluorescence signals were observed in tumor tissues after tTF-RGD treatments either through p.t. injection (Fig. 3I) or intravenous injection (Fig. 3J) compared to BSA and tTF treatments (Fig. 3, I and J). The major organs and tumors were collected for ex vivo imaging (fig. S8). A higher percentage of the signal was observed in tumor tissues in tTF-RGD group than tTF group. Collectively, these results substantiated that either p.t. or intravenous injection of tTF-RGD can actively recruit P-aPD-1 to the tumor site by selectively triggering thrombosis within tumor tissue.

In vivo antitumor efficacy of tTF-RGD + P-aPD-1 in a CT26 model

To study the antitumor efficacy of tTF-RGD + P-aPD-1 in vivo, we established a subcutaneous CT26 tumor model. When the tumor volume reached 100 to 150 mm^3, the mice were administered with different treatments, including saline, tTF-RGD, aPD-1, P-aPD-1, tTF + P-aPD-1, and tTF-RGD + P-aPD-1. First, we evaluated the therapeutic effect of the local treatment strategy, which leveraged p.t. injection of tTF-RGD to attract P-aPD-1 to the tumor site. After 0.5 hours after p.t. injection of tTF-RGD at the dose of 0.4 mg/kg, P-aPD-1 at the aPD-1 dose of 1 mg/kg was given by intravenous injection (Fig. 4A). As shown in Fig. 4 (B and C), tTF-RGD only showed negligible tumor-inhibiting activity against CT26 tumors. In addition, aPD-1 treatment strategies, including free aPD-1, P-aPD-1, and tTF + P-aPD-1, resulted in modest delayed tumor growth inhibition efficacy, leading to slightly increased survival time of CT26 tumor–bearing mice. As a comparison, tTF-RGD + P-aPD-1 exhibited the best tumor inhibition efficacy among all groups, which showed a significantly smaller tumor size than that in other treatment groups at day 24 (Fig. 4, B and C). Moreover, tTF-RGD + P-aPD-1 treatment notably prolonged the survival time of the mice to a median survival time of 58 days compared to saline (27 days), tTF-RGD (30 days), aPD-1 (31 days), P-aPD-1 (30 days), and tTF + P-aPD-1 (32 days) (Fig. 4D). Besides, the body weight of the mice were monitored throughout the time course of treatment, and no decrease in body weight after the treatment was observed, which demonstrated the in vivo biosafety profile of the strategy (fig. S9A). Notably, three of nine mice in the tTF-RGD + P-aPD-1 treatment group became tumor free. To substantiate the immune memory response after tTF-RGD + P-aPD-1 treatment, we rechallenged these tumor-free mice with 1×10^6 CT26-luc cells at day 70. Compared to the control naïve mice with progressive tumor growth, the treated mice did not develop visible tumors, and no obvious luciferase signal at the injection site was observed in bioluminescence images on day 12 after the rechallenge (Fig. 4, E and F) and later time point.

Next, we test the therapeutic effect of intravenously injected tTF-RGD + intravenously injected P-aPD-1. Encouraged by the potent treatment efficacy of p.t. tTF-RGD + intravenous P-aPD-1, we reduced the dose of aPD-1 to 0.3 mg/kg, which is a very low dose that systemically injected free antibodies almost show no effect. After 1 hour after intravenous injection of tTF-RGD (1.25 mg/kg), P-aPD-1 was administered by intravenous injection (Fig. 5A). tTF-RGD + P-aPD-1 showed the best performance in inhibiting tumor growth compared to all other treatment groups, in which the average tumor sizes in tTF-RGD + P-aPD-1 treatment groups are significantly smaller than those in other treatment groups on day 24 (Fig. 5, B and C). Besides, tTF-RGD + P-aPD-1 treatment prolonged the median survival time of the mice from 24 days (saline group) to 42 days, which is remarkably better than other groups (tTF-RGD: 27 days, aPD-1: 26 days, P-aPD-1: 30 days, and tTF + P-aPD-1: 29 days) (Fig. 5D). In addition, no body weight loss was observed after all treatments, evidencing the great safety profiles (fig. S9B).

Enhanced T cell infiltration after tTF-RGD + P-aPD-1 treatment

To investigate the underlying mechanism of the enhanced immunotherapy efficacy of our tTF-RGD + P-aPD-1 treatment strategy, the immune cell composition within the tumor tissue was profiled with a focus on examining $CD8^+$ effector T cell proportion. In the CT26 tumor–bearing mice after treatment with p.t. injection of tTF-RGD + intravenous injection of P-aPD-1 (aPD-1: 1 mg/kg), as shown in Fig. 6A, all aPD-1–based treatments increased the percentages of $CD8^+$ T cell population in $CD3^+$ T cells. Furthermore, the tTF-RGD + P-aPD-1 treatment showed the best efficacy in increasing the proportion of $CD3^+$ $CD8^+$ T cells among all treatment groups, which displayed a 1.33-fold increase compared to that in the tTF + P-aPD-1 treatment group and a 1.69-fold increase compared to that in the saline group (Fig. 6B). Quantitative immune cell analysis showed that the tTF-RGD + P-aPD-1 treatment induced a 1.89-fold increase in the number of $CD3^+$ $CD8^+$ T cells compared to the tTF + P-aPD-1 treatment and a 2.45-fold increase compared to the saline group (fig. S10). Moreover, the proportion of interferon-γ^+ (IFN-γ^+) $CD8^+$ T cells, which are recognized as effector $CD8^+$ T cells, was also remarkably increased after the treatment of tTF-RGD + P-aPD-1, which displayed a 1.60-fold increase compared to that in the tTF + P-aPD-1 treatment group and a 2.61-fold increase compared to that in the saline group (Fig. 6C). We then examined cytokines in the tumor tissues and found a marked elevation in antitumoral cytokines, such as tumor necrosis factor–α (TNF-α) and IFN-γ, after tTF-RGD + P-aPD-1 treatment (Fig. 6D).

We also examined the changes in T cell populations after intravenous injection of tTF-RGD + intravenous injection of P-aPD-1 in the CT26 tumor–bearing mice. Because of the very low dose of aPD-1 (0.3 mg/kg), treatment groups except for tTF-RGD + P-aPD-1 only showed negligible impact on $CD3^+$ $CD8^+$ T cell populations (Fig. 6E). On the contrary, the tTF-RGD + P-aPD-1 treatment remarkably increased $CD3^+$ $CD8^+$ T cell populations, which displayed a 1.44-fold increase compared to that the in tTF + P-aPD-1 treatment group and a 1.61-fold increase compared to that in the saline group (Fig. 6F). Quantitative analysis showed that the tTF-RGD + P-aPD-1 treatment contributed to a 2.04-fold increase in the number of $CD3^+$ $CD8^+$ T cells compared to the tTF + P-aPD-1 treatment and a 2.17-fold increase compared to the saline group (fig. S11). Moreover, the proportions of IFN-γ^+ $CD8^+$ T cells were remarkably increased after the treatment of tTF-RGD + P-aPD-1, which displayed a 1.59-fold increase compared to that in the

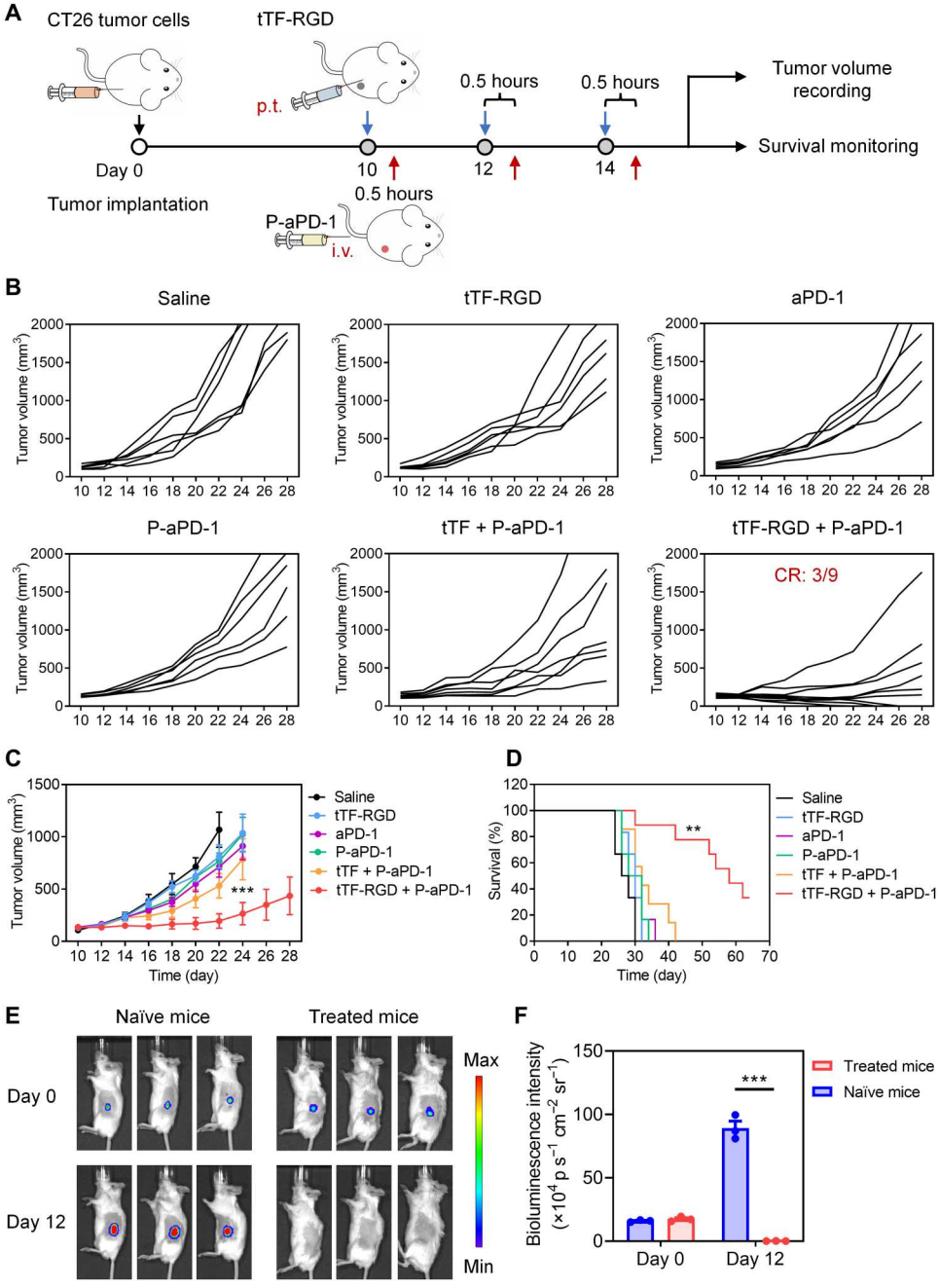

Fig. 4. Evaluation of therapeutic efficacy of p.t. injected tTF-RGD + intravenously injected P-aPD-1 in a CT26 subcutaneous tumor model. (**A**) Schematic illustration of the timeline of the CT26 tumor model establishment and treatment plan. i.v., intravenous. (**B**) Tumor growth of individual mice in different treatment groups (aPD-1 = 1 mg/kg and tTF or tTF-RGD = 0.4 mg/kg). Cure rate (CR) in the tTF-RGD + P-aPD-1 treatment group is 3/9. $n = 6$ to 9 per group. (**C**) Tumor volume changes after different treatments. Data are presented as means ± SEM. $^{***}P < 0.001$, two-way ANOVA followed by multiple comparison test. (**D**) Survival time of mice received different treatments. $^{**}P < 0.01$. Data were analyzed with log-rank test. (**E**) Bioluminescence images of naïve mice or tumor-free mice rechallenged with 1×10^6 of CT26-luc cells ($n = 3$). (**F**) Quantitative region-of-interest analysis of bioluminescence intensities in (E). Data are presented as means ± SEM. $^{***}P < 0.001$, unpaired Student's t tests.

tTF + P-aPD-1 treatment group and a 1.98-fold increase compared to that in the saline group (Fig. 6G). We then examined the levels of IFN-γ (Fig. 6H) and TNF-α (Fig. 6I) by enzyme-linked immunosorbent assay (ELISA). The results demonstrated a 2.83-fold increase in IFN-γ levels and a 2.04-fold increase in TNF-α levels in the tTF-RGD + P-aPD-1 treatment group compared with the saline group. The results suggested that the tTF-RGD + P-aPD-1 treatment promoted the secretion of these antitumoral cytokines.

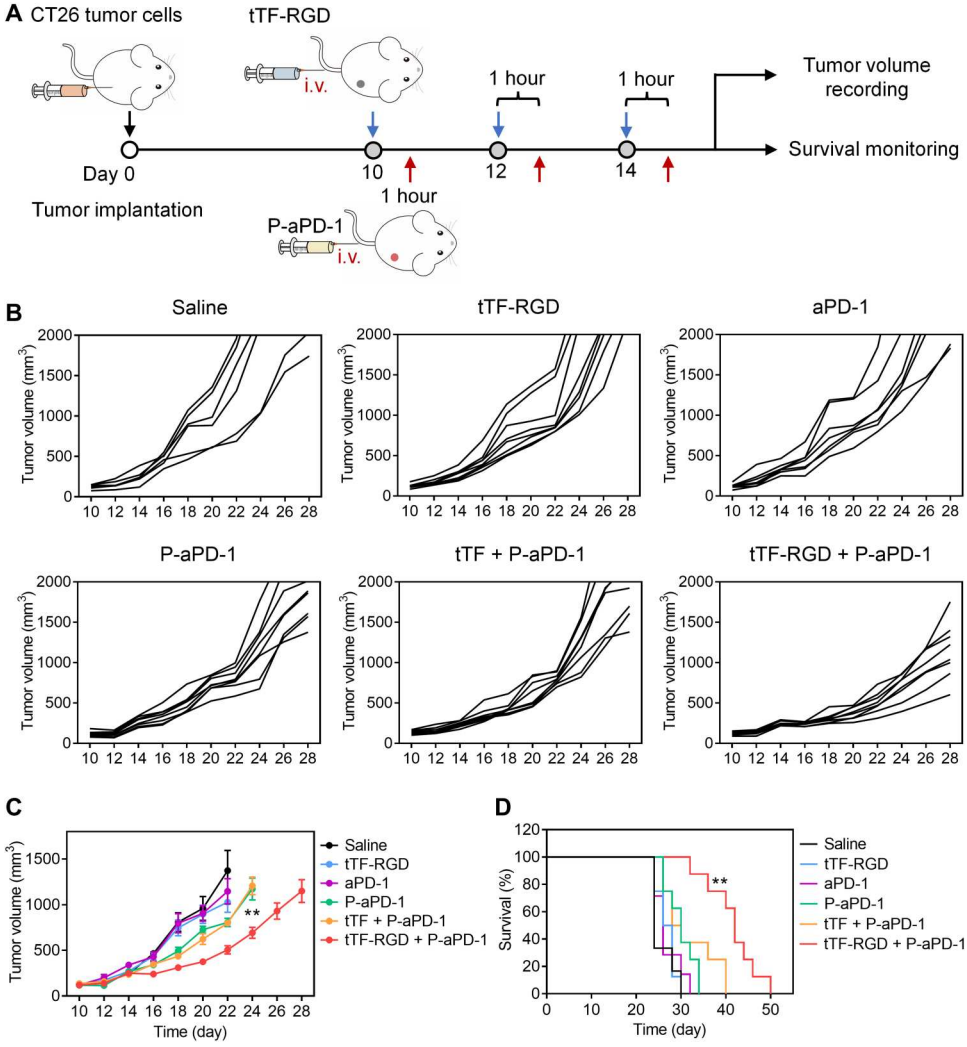

Fig. 5. Evaluation of therapeutic efficacy of intravenously injected tTF-RGD + intravenously injected P-aPD-1 in CT26 subcutaneous tumor model. (**A**) Schematic illustration of the timeline of the CT26 tumor model establishment and treatment plan. i.v., intravenous. (**B**) Tumor growth of individual mice in different treatment groups (aPD-1 = 0.3 mg/kg and tTF or tTF-RGD = 1.25 mg/kg). *n* = 6 to 8 per group. (**C**) Tumor volume changes after different treatments. Data are presented as means ± SEM. $^{**}P < 0.01$, two-way ANOVA followed by multiple comparison test. (**D**) Survival time of mice received different treatments. $^{**}P < 0.01$. Data were analyzed with log-rank test.

In vivo antitumor efficacy of tTF-RGD + P-aPD-1 in orthotopic 4T1 breast cancer models

Next, we evaluated the treatment efficacy of our strategies on orthotopic tumor models, which can better recapitulate the tumor microenvironment in real human tumor growth. Triple-negative breast cancers are reported to have a poor response to ICB therapy (*21*). Therefore, to further investigate the therapeutic potential of the strategies on orthotopic and nonimmunogenic breast tumors, we established 4T1 orthotopic breast cancer models by inoculating 4T1 cells into the mammary fat pad of the mice. When the tumor volume reached 100 to 150 mm^3, the mice were administered with different treatments, including saline, tTF-RGD, aPD-1, P-aPD-1, tTF + P-aPD-1, and tTF-RGD + P-aPD-1. First, we evaluated the therapeutic effect of the local treatment strategy, where P-aPD-1 at the aPD-1 dose of 1 mg/kg was administered via intravenous injection 0.5 hours after the p.t. injection of tTF-RGD (Fig. 7A). As shown in Fig. 7 (B and C), tTF-RGD did not show substantial tumor-inhibiting activity against 4T1 tumors. Treatment strategies based on aPD-1 antibodies, including free aPD-1, P-aPD-1, and tTF + P-aPD-1, slightly delayed tumor growth. Among all the treatment groups, tTF-RGD + P-aPD-1 exhibited the best tumor inhibition efficacy, which showed a notably smaller tumor size than that in other treatment groups on day 32 (Fig. 7B). Moreover, tTF-RGD + P-aPD-1 treatment showed the best efficacy in prolonging the survival time of the mice among all the treatment groups (Fig. 7C). Similarly, the systemic strategy of tTF-RGD + P-aPD-1 treatment showed the best performance in inhibiting tumor growth compared to all other treatment groups (Fig. 7, D and E). Besides, tTF-RGD + P-aPD-1 treatment prolonged the median survival time of the mice from 32 days (saline group) to 41 days, which is significantly better than other groups (tTF-RGD: 32 days, aPD-1: 34 days, P-aPD-1: 34 days, and tTF + P-aPD-1: 34 days) (Fig. 7F). No decrease in body weight of mice after the treatment was

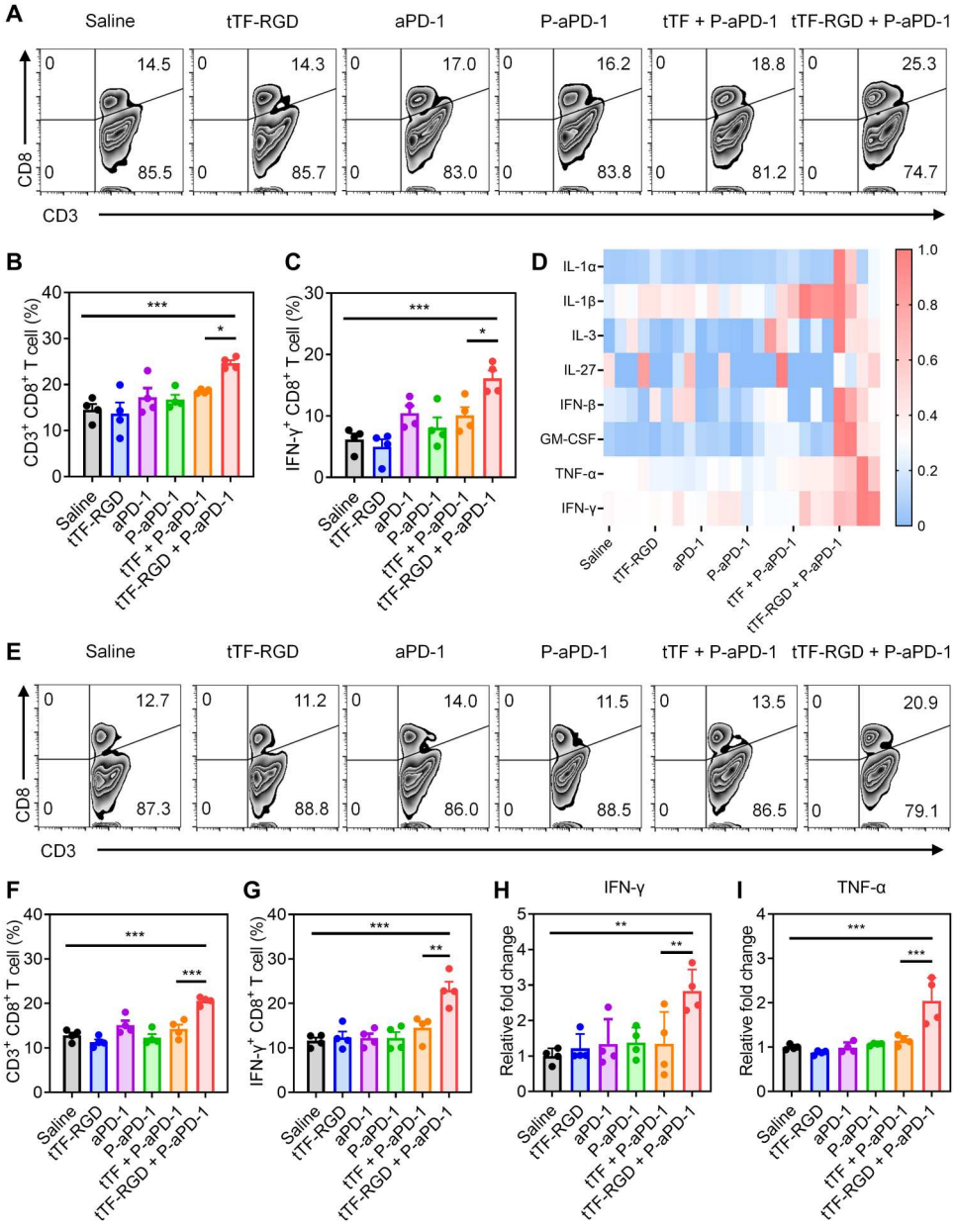

Fig. 6. Evaluation of the immunocellular composition and cytokine secretion after different treatments. (**A**) Representative flow cytometry plots of $CD8^+$ T cells (gated on $CD3^+$ T cells) in tumor tissues after the treatment of p.t. injected tTF-RGD (0.4 mg/kg) + intravenously injected P-aPD-1 (aPD-1: 1 mg/kg, platelet number: 1×10^8, $n = 4$). (**B**) Quantitative analysis of the percentage of $CD3^+$ $CD8^+$ T cells. (**C**) Percentage of interferon-γ^+ (IFN-γ^+) T cell populations in $CD3^+$ $CD8^+$ T cells. *$P < 0.05$; ***$P < 0.001$, one-way ANOVA followed by multiple comparison test. (**D**) Quantification of cytokine levels in treated tumors ($n = 4$). (**E**) Representative flow cytometry plots of $CD8^+$ T cells (gated on $CD3^+$ T cells) in tumor tissues after the treatment of intravenously injected tTF-RGD (1.25 mg/kg) + intravenously injected P-aPD-1 (aPD-1: 0.3 mg/kg, platelet number: 1×10^8, $n = 4$). (**F**) Quantitative analysis of the percentage of $CD3^+$ $CD8^+$ T cells. (**G**) Percentage of IFN-γ^+ T cell populations in $CD3^+$ $CD8^+$ T cells. (**H** and **I**) The levels of IFN-γ (H) and TNF-α (I) in tumor tissues ($n = 4$). Data are presented as means ± SEM. **$P < 0.01$; ***$P < 0.001$, one-way ANOVA followed by multiple comparison test.

observed, demonstrating the good biosafety profile of the tTF-RGD + P-aPD-1 strategy (fig. S12).

Recruitment of PM-NP to the tumor site by tTF-RGD in a PDX model

PMs inherited many surface receptors from platelets, and previous reports demonstrated that PM-cloaked NPs could migrate in response to platelet-attracting signals (*16*, *17*). Therefore, we hypothesized that the tTF-RGD–mediated platelet-recruiting strategy triggered by tumor-selective thrombosis could also be leveraged to guide the migration and accumulation of PM-cloaked NPs. To test this, modified dextran-based NPs were prepared using a single-emulsion method and then camouflaged with PMs (designated PM-NPs) as reported before (Fig. 8A) (*22*). The sizes of the NP and PM-NP were characterized by dynamic light scattering (DLS), which showed average sizes of 170.1 and 178.8 nm in

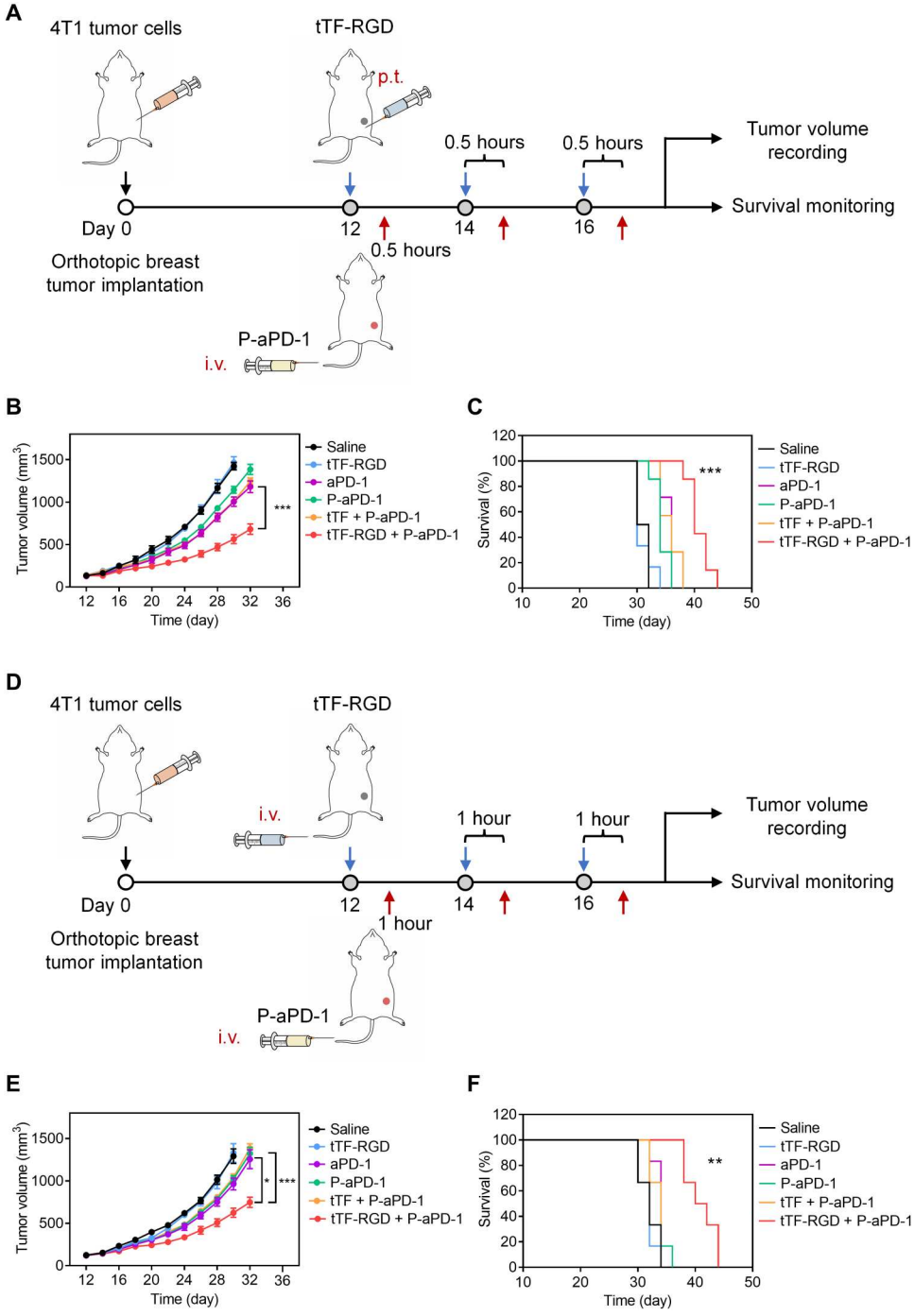

Fig. 7. Evaluation of therapeutic efficacy of p.t. or intravenously injected tTF-RGD + intravenously injected P-aPD-1 in 4T1 orthotopic breast cancer models. (**A**) Schematic illustration of the timeline of the 4T1 tumor model establishment and treatment plan with the local strategy. (**B**) Tumor volume changes after different treatments (aPD-1 = 1 mg/kg and tTF or tTF-RGD = 0.4 mg/kg). $n = 6$ to 7 per group. Data are presented as means ± SEM. ***$P < 0.001$, two-way ANOVA followed by multiple comparison test. (**C**) Survival time of mice received different treatments. ***$P < 0.001$, tTF-RGD + P-aPD-1 versus tTF + P-aPD-1 group. Data were analyzed with log-rank test. (**D**) Schematic illustration of the timeline of the 4T1 tumor model establishment and treatment plan with the systemic strategy. (**E**) Tumor volume changes after different treatments (aPD-1 = 1 mg/kg and tTF or tTF-RGD = 1.25 mg/kg). $n = 6$ per group. Data are presented as means ± SEM. *$P < 0.05$; ***$P < 0.001$, two-way ANOVA followed by multiple comparison test. (**F**) Survival time of mice received different treatments. **$P < 0.01$, tTF-RGD + P-aPD-1 versus tTF + P-aPD-1 group. Data were analyzed with log-rank test. i.v., intravenous.

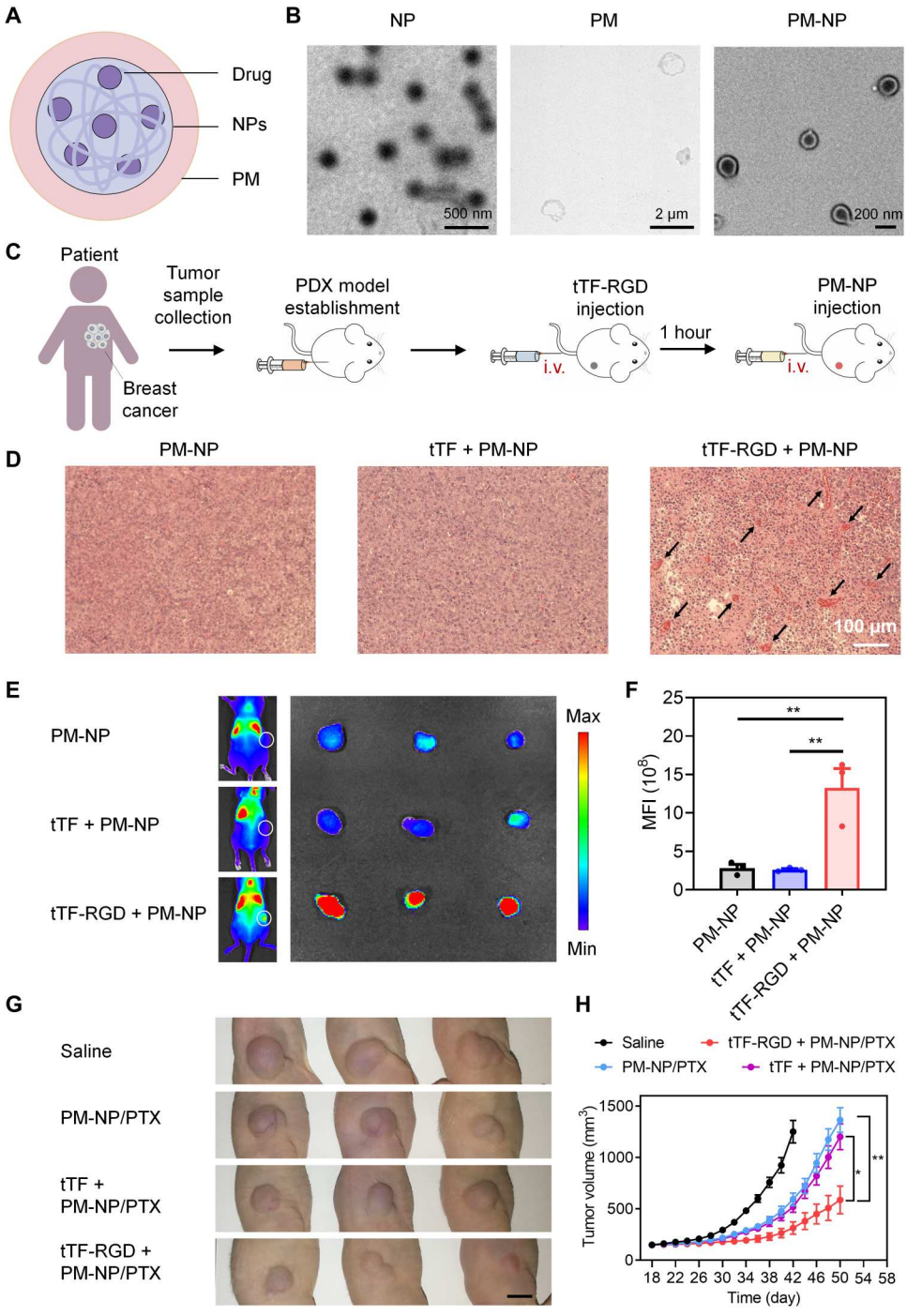

Fig. 8. Evaluation of therapeutic efficacy of intravenously injected tTF-RGD + intravenously injected PM-NP/PTX on a PDX breast cancer model. (**A**) Schematic illustration of the structure of platelet membrane (PM) cloaked–nanoparticle (NP). (**B**) Transmission electron microscopy (TEM) images of NPs, PM, and PM-NPs. (**C**) The establishment of the patient-derived xenograft (PDX) model on the immunodeficient mice and the tumor treatment plan. i.v., intravenous. (**D**) H&E staining of tumor tissues after receiving PM-NP, tTF + PM-NP, and tTF-RGD + PM-NP. Arrow indicates coagulation. (**E**) Fluorescence imaging of mice at 24 hours after intravenous injection of tTF/tTF-RGD + DiR-loaded PM-NP and the ex vivo images of tumors ($n = 3$). The white circle indicates the tumor site. (**F**) The MFIs of tumors shown in (E). $^{**}P < 0.01$, one-way ANOVA followed by multiple comparison test. (**G**) Photographs of tumors after different treatments on day 38. Scale bar, 1 cm. PTX, paclitaxel. (**H**) Tumor growth curve of mice received different treatments ($n = 7$ per group). Data are presented as means ± SEM. $^{*}P < 0.05$; $^{**}P < 0.01$, two-way ANOVA followed by multiple comparison test.

diameter, respectively (fig. S13). There was a slight increase in the size of NP after the decoration of PMs. Transmission electron microscopy (TEM) images showed a transparent layer outside the NPs, suggesting the successful coating of the PM onto NPs (Fig. 8B).

Next, we investigated whether tTF-RGD could recruit PM-NP to tumor sites. To validate the translational potential of our treatment strategy, we established a clinical-relevant PDX mouse model (Fig. 8C). We implanted TM00096 human breast tumor tissues on the right flank of the immunodeficient mice. To affirm that systemic injection of tTF-RGD can initiate the tumor-selective coagulation on the PDX model, tTF + PM-NP or tTF-RGD + PM-NP were administered to the mice via intravenous injection as described in the CT26 tumor–bearing mice model. Twenty-four hours later, the PDX tumors were collected and subjected to H&E staining. The results demonstrated that tTF-RGD could induce coagulation in PDX tumor tissues without severe hemorrhage, while no thrombosis was found in PM-NP and tTF + PM-NP treatment groups (Fig. 8D). To visualize the tumor-selective accumulation of PM-NP, 1,1'-dioctadecyl-3,3,3',3'-tetramethylindotricarbocyanine Iodide (DiR) dyes were encapsulated into NPs, which were further coated with PMs. The mice bearing PDX breast tumors received intravenous injection of tTF or tTF-RGD. One hour later, DiR-loaded PM-NP was injected via intravenous route. From the IVIS images shown in Fig. 8E, mice treated with tTF-RGD + PM-NP showed markedly enhanced accumulation of PM-NP at the tumor site at 24 hours compared to tTF + PM-NP and PM-NP treatment groups. Furthermore, the ex vivo quantification of MFI of tumors showed a 5.05-fold increase in the accumulation of PM-NP in mice treated with tTF-RGD than in those who received tTF treatments (Fig. 8F). Collectively, these results demonstrated that tTF-RGD that could induce tumor-specific coagulation was capable of enhancing the accumulation of PM-NPs at the tumor site.

In vivo antitumor efficacy of tTF-RGD+ PM-NP/PTX in a PDX model

The encouraging results of the augmented accumulation of PM-NP after the tTF-RGD treatment motivated us to examine its impact on the antitumor effect of drug-loaded PM-NPs. To expand the application of our treatment strategy to different therapeutical modalities, we prepared chemotherapeutic PTX-loaded PM-NP (designated PM-NP/PTX) and tested the therapeutic efficacy of tTF-RGD + PM-NP/PTX in the PDX model. The TM00096 breast cancer PDX model was established on immunodeficient mice. When the tumor volume reached 100 to 150 mm^3, the mice received different treatments, including saline, PM-NP/PTX, tTF + PM-NP/PTX, and tTF-RGD + PM-NP/PTX (tTF and tTF-RGD doses: 1.25 mg/kg and PTX dose: 2.5 mg/kg). As shown in Fig. 8 (G and H), PDX tumor–bearing mice in the saline group reached the maximized tumor burden allowed in our animal protocol (1500 mm^3) around day 40, while all the treatment groups with PM-NP/PTX suppressed tumor growth to various extents. Of note, tTF-RGD + PM-NP/PTX exhibited markedly better inhibition of tumor growth when compared to PM-NP/PTX and tTF + PM-NP/PTX treatments. Notably, the average tumor sizes in tTF-RGD + PM-NP/PTX on day 50 were 587.72 ± 135.29 mm^3, which was significantly smaller than those in tTF + PM-NP/PTX (1202.27 ± 125.58 mm^3) and PM-NP/PTX (1365.03 ± 120.06 mm^3). Besides, as shown in fig. S14, no substantial weight loss in the mice was observed after tTF-RGD + PM-NP/PTX treatments, suggesting the good safety profile of this treatment strategy. Together, the tTF-RGD–mediated coagulation facilitates the tumor accumulation of PM-NP/PTX, contributing to potent antitumor therapeutic efficacy.

DISCUSSION

In this work, we used tTF-RGD to initiate the coagulation cascade at the tumor site, which can recruit P-aPD-1 and PM-coated NPs to the tumor region. tTF-RGD targeted tumor neovasculature and initiated a coagulation cascade by mimicking the functionality of the TF. The tTF-RGD injected either by peritumoral or intravenous routes showed potent capability in triggering thrombus formation within the tumor region. P-aPD-1 was thereby recruited to the tumor area and subsequently activated to secrete PMPs and release aPD-1 antibodies locally. The strategy remarkably suppressed CT26 tumor growth and prolonged the survival time of CT26 tumor–bearing mice. Flow cytometry analysis revealed that the treatment increased $CD3^+$ $CD8^+$ T cell populations and the proportions of IFN-γ^+ $CD8^+$ T cells. Besides, the strategy improved the therapeutic efficacy of aPD-1 in 4T1 orthotopic breast cancer models. We then moved forward to explore whether PM-coated NPs could also migrate in response to tTF-RGD–mediated coagulation signaling. We prepared PM-NP/PTX and tested the tumor accumulation and antitumoral efficacy after tTF-RGD treatment on a PDX breast cancer model. Our results demonstrated that PM-NP/PTX could efficiently accumulate at the tumor site which was attributed to the attraction of platelets and platelet derivatives by tumor-selective thrombosis. Furthermore, this enhanced accumulation led to increased drug availability at the tumor site, thereby improving chemotherapy efficacy against PDX breast cancer.

In comparison with conventional targeted strategies based on ligand-receptor interaction, the tTF-RGD–mediated targeting strategy is anticipated to be less restricted by receptor saturation. By occupying a portion of receptors on cells, tTF-RGD can amplify the signals by inducing coagulation in the tumor area to attract substantial platelet-based therapeutics to the tumor site. Besides, both the dose and the administration intervals between tTF-RGD and platelet-based therapeutics can be adjusted, which provides flexible and dynamic control over the migration of therapeutics.

Cells are naturally smart components that can recognize and respond to physiological cues, which encourage the enthusiasm for developing cell-based delivery systems (*23*–*26*). Various surface receptors or other molecules enable cells to respond to physiological stimuli, allowing them to spontaneously target disease areas such as inflammatory or tumor sites (*27*–*29*). However, these properties on the other hand also restrict the potential of the cells, as their actions completely depend on the naturally existing cues. As a result, it remains difficult to communicate with cells or precisely manipulate their migration in vivo. For example, previous studies on platelet-based delivery systems are focused on preventing postsurgery tumor recurrence, because the formed inflammatory environment secondary to the surgical resection is favorable for platelet targeting and activation (*30*). Our study proposed a feasible strategy to navigate the migration of platelet-based therapeutics by inducing tumor-specific coagulation. The development of more artificially targeting environment for intelligent and controllable cell

migration will enhance the therapeutic potential of cell-based therapies (*31*, *32*).

One limitation of this study is to determine the most suitable amount of tTF-RGD theoretically. Direct intratumoral injection of a high concentration of tTF-RGD could induce severe thrombus, which may temporarily inhibit tumor growth by blocking tumor vasculature. However, whether this would cause the exclusion of immune cells such as T cells remains unknown. In addition, it is hard to predict the long-term impact on the angiogenesis of the tumor. We determined the experimental dose of tTF-RGD in this study by assessing the severity of coagulation from H&E staining and tumor morphology. However, more evaluation should be conducted when applying this strategy to other tumor types and species. Besides, further study may focus on mimicking the platelet-recruiting signals while only inducing modest coagulation, which will further overcome the potential limitations.

For clinical translation, many cell-based therapies such as chimeric antigen receptor T therapy are under clinical trial or have been approved for clinical use. Specifically, platelet infusion has been tested for decades, and it can be anticipated that platelet-based therapy may also exhibit a good biosafety profile. To test whether tTF-RGD can enhance the treatment outcome, we loaded a U.S. Food and Drug Administration–approved chemodrug PTX into PM-NP and tested its therapeutic efficacy on a PDX model. The results provide initial evidence that this strategy has potent efficacy and a good biosafety profile on a patient-related model. Furthermore, the cargoes in this versatile system can be replaced with other clinically available drugs, suggesting its promising wide application. More research on the pharmacokinetics, the maximum tolerable dose, and the long-term safety of tTF-RGD may further promote the translation of this platform. We hope that this work creates a paradigm of targeted therapy and generates more inspiration for developing locoregional treatment platforms to combat tumors.

MATERIALS AND METHODS

Antibodies, cells, and mice

The antibodies, including GoInVivo Purified anti-mouse CD279 (PD-1) antibody (clone no.: RMP1-14, category no.: 114114), allophycocyanin (APC)–anti-mouse CD3 (clone no.: 17A2, category no.: 100236), phycoerythrin (PE)–anti-mouse CD8a (clone no.: 53-6.7, category no.: 100708), and FITC–anti-mouse IFN-γ (clone no.: XMG1.2, category no.: 505806), were purchased from BioLegend. All antibody dilutions were performed according to the manufacturer′s guidance. The flow cytometry data were analyzed by FlowJo v10 software.

The mouse CT26 colon cancer cells were obtained from the American Type Culture Collection, and Luc-CT26 cells were purchased from Imanis Life Sciences Inc. Luciferase-tagged CT26 cells were used for in vivo bioluminescence imaging. TM00096 breast cancer tissue was obtained from the Jackson Laboratory. The Balb/c mice (female or male, aged 6 to 8 weeks) and nude mice (female, aged 6 to 8 weeks) were purchased from the Jackson Laboratory. The Rag2-Il2rg double-knockout mice (R2G2) mice (female, aged 6 to 8 weeks) were obtained from Envigo. The animal study protocol was approved by the Institutional Animal Care and Use Committee at the University of Wisconsin-Madison.

Expression, purification, and characterization of tTF and tTF-RGD

Full-length human TF amino acid sequence was obtained from UniProt (P13726). The cDNA encoding tTF containing amino acid 33 to 250 and the C-terminal extension (tTF-RGD) were synthesized by GenScript and then inserted into pET30a (+) vector using Bam HI and Nco I to generate tTF and tTF-RGD expression vector pET30a (+)–tTF and pET30a (+)–tTF-RGD. The tTF and tTF-RGD plasmids were introduced in *Escherichia coli* BL21(DE3) (Invitrogen), and the protein was purified with nickel–nitrilotriacetic acid (Ni-NTA) (QIAGEN).

tTF: Primer 1, 5′-CATGCCATGGGATCAGGCACTACAAA TACTGTG-3′; primer 2, 5′-CGGGATCCTATTATCT GAATTCCCCTTTC-3′.

tTF-RGD: Primer 1, 5′-CATGCCATGGGATCAGGCACTA CAAATACTGTG-3′; primer 3, 5′-CGGGATCCTATTATGGA GAATCACCTCTTCCTCTGAATTCCCC-3′.

A single colony of *E. coli* BL21(DE3) introduced with the vectors was selected and cultivated in the liquid LB medium containing kanamycin (50 μg/ml). When the optical density at 600 nm of bacteria solution reached ~0.6, 0.8 mM isopropyl-β-D-thiogalactopyranoside was added to induce the overexpression of the fusion protein. After ~6 hours, the cells were harvested and centrifuged at 2000*g* for 30 min at 4°C. Cells were suspended in lysis buffer and homogenized with a tissue grinder homogenizer. The cells were then incubated for 30 min at room temperature and centrifuged at 12,000*g* for 30 min at 4°C. The obtained pellet was resuspended in the washing buffer, followed by homogenization with a tissue grinder and sonication with the sonicate parameter (sonication time: 5 s, interval time: 5 s, 30 min in total). The mixture was centrifuged at 12,000*g* for 30 min at 4°C, and the supernatant was discarded. The procedure was repeated until the supernatant was clean. tTF and tTF-RGD proteins were extracted from washed pellets with a Ni-NTA column. The proteins in elution buffers were refolded by gradient dialysis against guanidinium chloride (GuCl) dialysis buffers containing a decreasing concentration of GuCl. The purity of tTF and tTF-RGD was tested using SDS-PAGE, and the concentration was determined with a bicinchoninic acid assay kit. The final proteins (>96% purity) were stored at −80°C.

The FX activation activity was tested using a modified procedure based on the previous report (*33*). Briefly, to each well of a black 96-well plate was added 100 μl of BSA, tTF, and tTF-RGD with different concentrations in tris-buffered saline containing 0.1% BSA. Then, 10 μl of FVIIa solution (Haematologic Technologies Inc.) was added, followed by the rapid addition of 10 μl of 50 nM $CaCl_2$ and 500 μM phospholipids. After 5 min of incubation at room temperature, FX (Haematologic Technologies Inc.) was added to reach a final concentration of 30 nM and reacted for an additional 5 min. The reaction was quenched by the addition of 20 μl of EDTA solution (100 mmol/liter) before 10 μl of 6-amino-1-naphthalenesulfonamide–based fluorogenic substrate (10 mM) (Haematologic Technologies Inc.) was added to the mixture. Three minutes later, the fluorescence intensities were measured with a microplate reader (excitation wavelength = 352 nm and emission wavelength = 470 nm).

Tumor vasculature–targeting and coagulation-initiating ability of tTF-RGD

The tumor vasculature–targeting ability of tTF-RGD was investigated using IVIS. Briefly, tTF and tTF-RGD were labeled with Sulfo-Cy5.5 *N*-hydroxysuccinimide (NHS) ester and dialyzed against phosphate-buffered saline (PBS) at 4°C to remove unreacted dyes. Balb/c mice (male, aged 6 to 8 weeks) were inoculated with 1×10^6 CT26 cells. When the tumor volumes reached 100 to 150 mm^3 (calculated as length × width^2 × 0.5), Cy5.5-labeled tTF or tTF-RGD were injected at the dose of 1.25 mg/kg via intravenous route to mice bearing CT26 tumors. The biodistribution of tTF or tTF-RGD was observed at different time points. At 24 hours, the mice were euthanized, and tumors were collected and visualized ex vivo. The fluorescence was analyzed using Living Image Software v.4.3.1 (PerkinElmer).

To assess the tumor vasculature coagulation triggered by tTF-RGD, fibrinogen was labeled with Sulfo-Cy5.5 NHS ester and dialyzed against PBS to remove unreacted dyes. BSA, tTF, or tTF-RGD were injected at the dose of 1.25 mg/kg via intravenous route to mice bearing CT26 tumors, followed by intravenous injection of 1 nmol of fibrinogen. The biodistribution of fibrinogen was observed at different time points. At 24 hours, the mice were euthanized, and tumors and organs were collected and visualized ex vivo.

The coagulation initiation capability of tTF-RGD was investigated by treating CT26 tumor-bearing mice with BSA, tTF, and tTF-RGD (1.25 mg/kg) via intratumoral injection. Twenty-four hours later, the tumors were collected and subjected to H&E staining. To characterize the coagulation triggered by a lower dose of tTF-RGD, BSA, tTF, and tTF-RGD (0.4 mg/kg) were administered into CT26 tumor–bearing mice via p.t. injection. Furthermore, mice bearing CT26 tumors were also treated with BSA, tTF, and tTF-RGD (1.25 mg/kg) via intravenous route every other day for three times in total. Twenty-four hours after injection of the last dose, the tumors and other major organs were collected and subjected to H&E staining.

Preparation and characterization of P-aPD-1

The platelets were isolated from whole mouse blood by gradient centrifugation. The collected blood was centrifuged for 20 min at 100*g* twice to remove red blood cells, followed by centrifugation for 20 min at 1500*g* to isolate platelets. The platelets were resuspended in PBS containing 1 μM prostaglandin E_1. To prepare P-aPD-1, aPD-1 antibodies and Sulfo-SMCC linkers were mixed at a molar ratio of 1:1.2 and stirred at 4°C. Two hours later, the solution was centrifuged in ultrafiltration tubes (3000-kDa molecular weight cutoff) at 4°C to remove the unbound linkers. The SMCC–aPD-1 was reacted with Traut's reagent–treated platelets at room temperature for 1 hour, followed by removing the excess antibodies using centrifugation at 1500*g* for 20 min. The amount of the conjugated aPD-1 was measured using rat immunoglobulin G (IgG) total ELISA kit after applying 0.1% Triton X-100 solution to release the antibody under sonication.

To verify the conjugation of aPD-1 and platelets, aPD-1 stained with FITC and platelets stained with WGA 594 were used to prepare P-aPD-1 and were observed under the confocal microscope. To study the thrombin-triggered aggregation of platelets, rhodamine B–labeled P-aPD-1 or platelets were cultured in a complete medium supplemented with thrombin (0.5 U/ml) and then visualized using the confocal microscope. To study the collagen binding capability, confocal dishes were coated with collagen (1.0 mg/ml; Sigma-Aldrich) overnight at 4°C. BSA (2%) in PBS was used to block the coated or uncoated confocal dishes. Platelets or P-aPD-1 labeled with rhodamine B were then incubated in the dishes for 5 min. The dishes were washed with PBS to remove the unbound platelets or P-aPD-1 and then visualized using the confocal microscope.

To study the release of aPD-1, 1×10^8 of P-aPD-1 was suspended in 500 μl of PBS before thrombin (0.5 U/ml) was added to activate the platelets. The suspension was placed at 37°C, and 50 μl of samples were collected at prearranged time intervals. The samples were centrifuged at 1500*g* for 10 min, and the aPD-1 in the supernatant was measured using rat IgG total ELISA kit. Nonactivated P-aPD-1 was used as control.

Recruitment of P-aPD-1 by tTF-RGD treatment

The recruitment of P-aPD-1 to tumor sites by tTF-RGD–initiated coagulation was studied using IVIS. P-aPD-1 was reacted with Sulfo-Cy5.5 NHS ester at room temperature for 1 hour and washed three times with PBS to remove unreacted dyes. For the local treating strategy, BSA, tTF, and tTF-RGD were given at the dose of 0.4 mg/kg via p.t. injection to mice bearing CT26 tumors, followed by intravenous injection of P-aPD-1 (platelet number: ~1×10^8). For the systemic treatment strategy, BSA, tTF, and tTF-RGD were given at the dose of 1.25 mg/kg via intravenous injection to mice bearing CT26 tumors, followed by intravenous injection of P-aPD-1 (platelet number: ~1×10^8). The biodistribution of P-aPD-1 was observed at different time points. At 24 hours, the mice were euthanized, and tumors were collected and visualized ex vivo.

To examine the distribution of P-aPD-1, P-aPD-1 was labeled with rhodamine B and given by intravenous injection following the p.t./intravenous injection of BSA, tTF, or tTF-RGD. At 24 hours, the tumors were collected from the mice and subjected to frozen section. The cell nuclei were stained with Hoechst 33342, and the section slides were observed under the confocal microscope.

Anti-tumor efficacy of tTF-RGD + P-aPD-1

To establish a subcutaneous CT26 colon cancer model, Balb/c mice (male, aged 6 to 8 weeks) were subcutaneously inoculated with 1×10^6 CT26 cells on the right flank. When the tumor volume reached 100 to 150 mm^3, the mice received different treatments, including saline, aPD-1, tTF-RGD, P-aPD-1, tTF + P-aPD-1, and tTF-RGD + P-aPD-1. For the local treating strategy, tTF or tTF-RGD (0.4 mg/kg) was first given by p.t. injection. Half an hour later, P-aPD-1 was administered via intravenous injection at the aPD-1 dose of 1 mg/kg. The treatment was conducted every other day for three times in total. For the systemic treating strategy, tTF or tTF-RGD (1.25 mg/kg) was first given by intravenous injection. One hour later, P-aPD-1 was administered via intravenous injection at the aPD-1 dose of 0.3 mg/kg. The treatment was conducted every other day for three times in total. The antibodies used in other treatment groups are also given at an equivalent dose. The tumor growth (calculated as length × width^2 × 0.5), and body weight was monitored every other day. Mice were euthanized once the tumor volume exceeded 2000 mm^3.

The 4T1 orthotopic breast cancer model was established by inoculating with 1×10^6 4T1 cells into the mammary fat pad of Balb/c mice (female, aged 6 to 8 weeks). When the tumor volume reached

100 to 150 mm^3, the mice received different treatments, including saline, aPD-1, tTF-RGD, P-aPD-1, tTF + P-aPD-1, and tTF-RGD + P-aPD-1. The treatment timeline and the doses of tTF-RGD were consistent with those for the CT26 tumor treatment. P-aPD-1 was administered via intravenous injection at the aPD-1 dose of 1 mg/kg. The tumor growth and body weight were monitored every other day. Mice were euthanized once the tumor volume exceeded 1500 mm^3.

Tumor tissues were collected on day 12 after the first treatment, digested with collagenase, and filtered through cell strainers with pore sizes of 40 μm to obtain single-cell suspension. The cells were collected by centrifugation, and the supernatant was used for the detection of cytokines. The cells were resuspended in PBS, stained with APC–anti-mouse CD3 and PE–anti-mouse CD8a, and analyzed using flow cytometry. The staining of FITC–anti-mouse IFN-γ was conducted according to the BioLegend intracellular flow cytometry staining protocol. $CD3^+CD8^+$ cells were quantified with precision count beads (BioLegend, 424902) according to the manufacturer's guidance.

The tumor tissue supernatant after centrifugation was used for the detection of IFN-γ and TNF-α with the corresponding ELISA kits. The fold change was calculated for cytokine levels after different treatments relative to the saline group. Interleukin-1α (IL-1α), IL-1β, IL-3, IL-27, IFN-β, and granulocyte-macrophage colony-stimulating factor were tested using LEGENDplex Mouse Cytokine Panel 2 (BioLegend, 740134) according to the guidance of manufacturers.

Synthesis of dextran NP and preparation and characterization of PM-NP

Modified dextran was synthesized according to our previous report (*34*). Briefly, 1.0 g of dextran [number-average molecular weight (M_n) ~9 to 11 kDa] was dissolved in 10 ml of dimethyl sulfoxide. Then, 15.6 mg of pyridinium *p*-toluenesulfonate and 4.16 ml of 2-ethoxypropene were added to the solution and stirred for 30 min at room temperature. Afterward, 1 ml of triethylamine was added to quench the reaction. The precipitated mixture was washed in basic water (pH ~8) before lyophilization.

Dextran NPs were prepared using a single-emulsion method. Briefly, 10 mg of modified dextran and 0.5 mg of PTX were dissolved in 2 ml of dichloromethane (DCM), followed by the addition of 4 ml of 3% poly(vinyl alcohol) (PVA) solution. The mixture was subjected to sonication for 2 min (percent amplification, 35%; 2 s on and 2 s off circles) before being dispersed in 20 ml of 0.3% PVA solution. The solution was stirred to evaporate the DCM. NPs were collected by centrifugation and washed twice to remove unencapsulated drugs. To load the NIR dyes into NPs, 10 mg of modified dextran and 0.1 mg of DiR were used to prepare DiR-loaded NPs with the same procedures as described above.

To prepare PM-NPs, first, platelets isolated from whole mouse blood were diluted with sterile ddH_2O and disrupted with ultrasonication. The PMs were centrifuged at 4500*g* for 5 min and washed twice with sterile ddH_2O. The pH of the solution was adjusted to 7. The PMs and NPs were sonicated together for 30 s (percent amplification, 35%; 2 s on and 2 s off circles) before stirring for 3 hours at room temperature. The formed PM-NP was centrifuged at 13,800*g* for 30 min and washed with ddH_2O. The NPs were diluted in sterile saline for in vivo study. The morphologies of NPs and PM-NPs were observed under TEM, and their sizes were tested by DLS. The drug encapsulation efficiency was determined by high-performance liquid chromatography.

Establishment of the PDX model

To establish the PDX model, TM00096 tumor samples were first propagated on R2G2 mice (female, aged 6 to 8 weeks) and then passaged to nude mice (female, aged 6 to 8 weeks). Briefly, tumor tissues from R2G2 mice with TM00096 tumors were cut into small pieces and dispersed in the 1:1 mixture of Dulbecco's modified Eagle's medium and Matrigel supplemented with fetal bovine serum and antibiotics. The tiny tumor tissues were mixed thoroughly and placed on ice packs before being injected into the right flank of the nude mice using an 18-gauge needle (100 μl per mouse).

Recruitment of PM-NP by tTF-RGD–triggered coagulation

The recruitment of PM-NPs to tumor sites by tTF-RGD–initiated coagulation was studied using IVIS. NPs were loaded with DiR and coated with PMs. The PM-NP was washed three times with PBS to remove unreacted dyes. tTF or tTF-RGD was given at the dose of 1.25 mg/kg via intravenous injection to mice bearing PDX breast tumors. One hour later, 2 mg of NPs and PM-NPs were administered via intravenous injection. The biodistribution of NP and PM-NP was observed at different time points. At 24 hours, the mice were euthanized, and tumors were collected and visualized ex vivo.

Antitumor efficacy of tTF-RGD + PM-NP/PTX

The PDX breast tumor model was established as described before. When the tumor volumes reached 100 to 150 mm^3, the mice were randomly grouped and received different treatments, including saline, PM-NP/PTX, tTF + PM-NP/PTX, and tTF-RGD + PM-NP/PTX. tTF or tTF-RGD (1.25 mg/kg) was first given by intravenous injection. One hour later, PM-NP/PTX was administered via intravenous injection at the PTX dose of 2.5 mg/kg. The treatment was conducted every other day for three times in total. The tumor volume (calculated as length × $width^2$ × 0.5) and body weight change were monitored. Mice were euthanized once the tumor volume exceeded 1500 mm^3.

Statistical analysis

All the results are shown as means ± SEM. Statistical analysis was performed using GraphPad Prism (version 9), and analysis of variance (ANOVA) was used to compare multiple groups statistically. Survival studies were analyzed using log-rank test. A P value lower than 0.05 ($^*P < 0.05$) was defined as statistically significant; $^*P < 0.05$; $^{**}P < 0.01$; $^{***}P < 0.001$.

Supplementary Materials

This PDF file includes:

Figs. S1 to S14

View/request a protocol for this paper from *Bio-protocol*.

REFERENCES AND NOTES

1. R. J. Motzer, B. Escudier, D. F. McDermott, S. George, H. J. Hammers, S. Srinivas, S. S. Tykodi, J. A. Sosman, G. Procopio, E. R. Plimack, D. Castellano, T. K. Choueiri, H. Gurney, F. Donskov, P. Bono, J. Wagstaff, T. C. Gauler, T. Ueda, Y. Tomita, F. A. Schutz, C. Kollmannsberger, J. Larkin, A. Ravaud, J. S. Simon, L. A. Xu, I. M. Waxman, P. Sharma; Checkmate 025

Investigators, Nivolumab versus everolimus in advanced renal-cell carcinoma. *N. Engl. J. Med.* **373**, 1803–1813 (2015).
2. A. M. Zeidan, P. C. Boddu, B. L. Wood, D. Zelterman, R. F. Little, S. P. Ivy, A. Caldwell, B. Sanchez-Espiridion, G. Alatrash, E. Sharon, J. P. Radich, Blast MRD AML-1 trial: Blockade of PD-1 added to standard therapy to target measurable residual disease in acute myeloid leukemia (AML) 1-an investigator-initiated, CTEP-sponsored, randomized phase 2 study of the anti-PD-1 antibody pembrolizumab in combination with conventional intensive chemotherapy (IC) as frontline therapy in patients with acute myeloid leukemia (AML). *Blood* **136**, 15 (2020).
3. J. Ishihara, A. Ishihara, K. Sasaki, S. S. Y. Lee, J. M. Williford, M. Yasui, H. Abe, L. Potin, P. Hosseinchi, K. Fukunaga, M. M. Raczy, L. T. Gray, A. Mansurov, K. Katsumata, M. Fukayama, S. J. Kron, M. A. Swartz, J. A. Hubbell, Targeted antibody and cytokine cancer immunotherapies through collagen affinity. *Sci. Transl. Med.* **11**, eaau3259 (2019).
4. S. L. Topalian, F. S. Hodi, J. R. Brahmer, S. N. Gettinger, D. C. Smith, D. F. McDermott, J. D. Powderly, R. D. Carvajal, J. A. Sosman, M. B. Atkins, P. D. Leming, D. R. Spigel, S. J. Antonia, L. Horn, C. G. Drake, D. M. Pardoll, L. P. Chen, W. H. Sharfman, R. A. Anders, J. M. Taube, T. L. McMiller, H. Y. Xu, A. J. Korman, M. Jure-Kunkel, S. Agrawal, D. McDonald, G. D. Kollia, A. Gupta, J. M. Wigginton, M. Sznol, Safety, activity, and immune correlates of anti-PD-1 antibody in cancer. *N. Engl. J. Med.* **366**, 2443–2454 (2012).
5. Y. K. Chae, A. Arya, W. Iams, M. R. Cruz, S. Chandra, J. Choi, F. Giles, Current landscape and future of dual anti-CTLA4 and PD-1/PD-L1 blockade immunotherapy in cancer; lessons learned from clinical trials with melanoma and non-small cell lung cancer (NSCLC). *J. Immunother. Cancer* **6**, 39 (2018).
6. X. X. Du, M. Y. Liu, J. J. Su, P. Zhang, F. Tang, P. Y. Ye, M. Devenport, X. Wang, Y. Zhang, Y. Liu, P. Zheng, Uncoupling therapeutic from immunotherapy-related adverse effects for safer and effective anti-CTLA-4 antibodies in CTLA4 humanized mice. *Cell Res.* **28**, 433–447 (2018).
7. C. R. Gurbatri, I. Lia, R. Vincent, C. Coker, S. Castro, P. M. Treuting, T. E. Hinchliffe, N. Arpaia, T. Danino, Engineered probiotics for local tumor delivery of checkpoint blockade nanobodies. *Sci. Transl. Med.* **12**, eaax0876 (2020).
8. D. M. Francis, M. P. Manspeaker, A. Schudel, L. F. Sestito, M. J. O'Melia, H. T. Kissick, B. P. Pollack, E. K. Waller, S. N. Thomas, Blockade of immune checkpoints in lymph nodes through locoregional delivery augments cancer immunotherapy. *Sci. Transl. Med.* **12**, eaay3575 (2020).
9. A. Marabelle, R. Andtbacka, K. Harrington, I. Melero, R. Leidner, T. de Baere, C. Robert, P. A. Ascierto, J. F. Baurain, M. Imperiale, S. Rahimian, D. Tersago, E. Klumper, M. Hendriks, R. Kumar, M. Stern, K. Ohrling, C. Massacesi, I. Tchakov, A. Tse, J. Y. Douillard, J. Tabernero, J. Haanen, J. Brody, Starting the fight in the tumor: Expert recommendations for the development of human intratumoral immunotherapy (HIT-IT). *Ann. Oncol.* **29**, 2163–2174 (2018).
10. I. Melero, E. Castanon, M. Alvarez, S. Champiat, A. Marabelle, Intratumoural administration and tumour tissue targeting of cancer immunotherapies. *Nat. Rev. Clin. Oncol.* **18**, 558–576 (2021).
11. B. Jeschke, J. Meyer, A. Jonczyk, H. Kessler, P. Adamietz, N. M. Meenen, M. Kantlehner, C. Goepfert, B. Nies, RGD-peptides for tissue engineering of articular cartilage. *Biomaterials* **23**, 3455–3463 (2002).
12. S. Kwon, S. Ke, J. P. Houston, W. Wang, Q. Wu, C. Li, E. M. Sevick-Muraca, Imaging dose-dependent pharmacokinetics of an RGD-fluorescent dye conjugate targeted to $\alpha_v\beta_3$ receptor expressed in Kaposi's sarcoma. *Mol. Imaging* **4**, 75–87 (2005).
13. T. A. Petrie, J. R. Capadona, C. D. Reyes, A. J. Garcia, Integrin specificity and enhanced cellular activities associated with surfaces presenting a recombinant fibronectin fragment compared to RGD supports. *Biomaterials* **27**, 5459–5470 (2006).
14. R. Bieker, T. Kessler, C. Schwoppe, T. Padro, T. Persigehl, C. Bremer, J. Dreischaluck, A. Kolkmeyer, W. Heindel, R. M. Mesters, W. E. Berdel, Infarction of tumor vessels by NGR-peptide-directed targeting of tissue factor: Experimental results and first-in-man experience. *Blood* **113**, 5019–5027 (2009).
15. Q. Y. Hu, W. J. Sun, C. G. Qian, H. N. Bomba, H. L. Xin, Z. Gu, Relay drug delivery for amplifying targeting signal and enhancing anticancer efficacy. *Adv. Mater.* **29**, 1605803 (2017).
16. C. M. J. Hu, R. H. Fang, K. C. Wang, B. T. Luk, S. Thamphiwatana, D. Dehaini, P. Nguyen, P. Angsantikul, C. H. Wen, A. V. Kroll, C. Carpenter, M. Ramesh, V. Qu, S. H. Patel, J. Zhu, W. Shi, F. M. Hofman, T. C. Chen, W. W. Gao, K. Zhang, S. Chien, L. F. Zhang, Nanoparticle biointerfacing by platelet membrane cloaking. *Nature* **526**, 118–121 (2015).
17. Q. Y. Hu, W. J. Sun, C. G. Qian, C. Wang, H. N. Bomba, Z. Gu, Anticancer platelet-mimicking nanovehicles. *Adv. Mater.* **27**, 7043–7050 (2015).
18. G. von Maltzahn, J. H. Park, K. Y. Lin, N. Singh, C. Schwoppe, R. Mesters, W. E. Berdel, E. Ruoslahti, M. J. Sailor, S. N. Bhatia, Nanoparticles that communicate in vivo to amplify tumour targeting. *Nat. Mater.* **10**, 545–552 (2011).
19. P. E. J. van der Meijden, J. W. M. Heemskerk, Platelet biology and functions: New concepts and clinical perspectives. *Nat. Rev. Cardiol.* **16**, 166–179 (2019).
20. S. R. Coughlin, How the protease thrombin talks to cells. *Proc. Natl. Acad. Sci. U.S.A.* **96**, 11023–11027 (1999).
21. G. Bianchini, J. M. Balko, I. A. Mayer, M. E. Sanders, L. Gianni, Triple-negative breast cancer: Challenges and opportunities of a heterogeneous disease. *Nat. Rev. Clin. Oncol.* **13**, 674–690 (2016).
22. Q. Y. Hu, C. G. Qian, W. J. Sun, J. Q. Wang, Z. W. Chen, H. N. Bomba, H. L. Xin, Q. D. Shen, Z. Gu, Engineered nanoplatelets for enhanced treatment of multiple myeloma and thrombus. *Adv. Mater.* **28**, 9573–9580 (2016).
23. X. Gong, J. Li, T. Tan, Z. W. Wang, H. Wang, Y. Q. Wang, X. X. Xu, Z. W. Zhang, Y. P. Li, Emerging approaches of cell-based nanosystems to target cancer metastasis. *Adv. Funct. Mater.* **29**, 1903441 (2019).
24. J. W. Xue, Z. K. Zhao, L. Zhang, L. J. Xue, S. Y. Shen, Y. J. Wen, Z. Y. Wei, L. Wang, L. Y. Kong, H. B. Sun, Q. N. Ping, R. Mo, C. Zhang, Neutrophil-mediated anticancer drug delivery for suppression of postoperative malignant glioma recurrence. *Nat. Nanotechnol.* **12**, 692–700 (2017).
25. Q. Y. Hu, W. J. Sun, J. Q. Wang, H. T. Ruan, X. D. Zhang, Y. Q. Ye, S. Shen, C. Wang, W. Y. Lu, K. Cheng, G. Dotti, J. F. Zeidner, J. Wang, Z. Gu, Conjugation of haematopoietic stem cells and platelets decorated with anti-PD-1 antibodies augments anti-leukaemia efficacy. *Nat. Biomed. Eng.* **2**, 831–840 (2018).
26. X. C. Hou, X. F. Zhang, W. Y. Zhao, C. X. Zeng, B. B. Deng, D. W. McComb, S. Du, C. X. Zhang, W. Q. Li, Y. Z. Dong, Vitamin lipid nanoparticles enable adoptive macrophage transfer for the treatment of multidrug-resistant bacterial sepsis. *Nat. Nanotechnol.* **15**, 41–46 (2020).
27. S. Im, D. Jang, G. Saravanakumar, J. S. Lee, Y. Kang, Y. M. Lee, J. Y. Lee, J. Doh, Z. Y. Yang, M. H. Jang, W. J. Kim, Harnessing the formation of natural killer–tumor cell immunological synapses for enhanced therapeutic effect in solid tumors. *Adv. Mater.* **32**, 2000020 (2020).
28. J. M. Karp, G. S. L. Teo, Mesenchymal stem cell homing: The devil is in the details. *Cell Stem Cell* **4**, 206–216 (2009).
29. M. R. Reagan, D. L. Kaplan, Concise review: Mesenchymal stem cell tumor-homing: detection methods in disease model systems. *Stem Cells* **29**, 920–927 (2011).
30. C. Wang, W. J. Sun, Y. Q. Ye, Q. Y. Hu, H. N. Bomba, Z. Gu, In situ activation of platelets with checkpoint inhibitors for post-surgical cancer immunotherapy. *Nat. Biomed. Eng.* **1**, 0011 (2017).
31. J. X. Fan, X. H. Liu, X. N. Wang, M. T. Niu, Q. W. Chen, D. W. Zheng, J. S. Wei, X. Q. Yang, X. Zeng, X. Z. Zhang, Antibody engineered platelets attracted by bacteria-induced tumor-specific blood coagulation for checkpoint inhibitor immunotherapy. *Adv. Funct. Mater.* **31**, 2009744 (2021).
32. H. J. Li, Z. J. Wang, Z. W. Chen, T. Y. Ci, G. J. Chen, D. Wen, R. X. Li, J. Q. Wang, H. Meng, R. B. Bell, Z. F. Gu, G. Dotti, Z. Gu, Disrupting tumour vasculature and recruitment of aPDL1-loaded platelets control tumour metastasis. *Nat. Commun.* **12**, 2773 (2021).
33. W. Ruf, A. Rehemtulla, T. S. Edgington, Phospholipid-independent and -dependent interactions required for tissue factor receptor and cofactor function. *J. Biol. Chem.* **266**, 2158–2166 (1991).
34. Z. Li, Y. Ding, J. Liu, J. Wang, F. Mo, Y. Wang, T. J. Chen-Mayfield, P. M. Sondel, S. Hong, Q. Hu, Depletion of tumor associated macrophages enhances local and systemic platelet-mediated anti-PD-1 delivery for post-surgery tumor recurrence treatment. *Nat. Commun.* **13**, 1845 (2022).

Acknowledgments: We acknowledge G. Kwon's lab for the help with NP characterization. We also thank the optical imaging core, small animal facilities, flow cytometry core, and histological core at the University of Wisconsin-Madison for their help with this study. **Funding:** This work was supported by P30CA014520-UW Carbone Cancer Center Support Grant (CCSG) and the start-up package from the University of Wisconsin-Madison (to Q.H.). **Author contributions:** Conceptualization: Y.W. and Q.H. Methodology: Y.W., W.L., Z.L., F.M., Y.C., M.I., and D.L.W. Investigation: Y.W., W.L., and F.M. Visualization: Y.W. Funding acquisition: Q.H. Project administration: Y.W. Supervision: Q.H. Writing: Y.W. and Q.H. **Competing interests:** Q.H. and Y.W. are inventors on a patent application related to this work filed by the University of Wisconsin-Madison (no. 63423884, filed 9 November 2022). The authors declare that they have no other competing interests. **Data and materials availability:** All data needed to evaluate the conclusions in the paper are present in the paper and/or the Supplementary Materials.

Submitted 6 November 2022
Accepted 1 March 2023
Published 29 March 2023
10.1126/sciadv.adf6854